Signal-Injection Sensorless Control of Synchronous Reluctance Machines for Overload Operation

Signal-Injection Sensorless Control of Synchronous Reluctance Machines for Overload Operation

Anantaram Varatharajan, *Member, IEEE,* Gianmario Pellegrino, *Senior Member, IEEE,* and Eric Armando, *Senior Member, IEEE,*

***Abstract*—Signal-injection sensorless control (SISC) for low speeds region are usually assisted with compensation techniques to support the heavy load operations beyond rated conditions. For the standard d-axis pulsating voltage injection, this paper analyzes the prospect of using q-axis current-model flux instead of the q-axis current for decoupled position estimation. Through convergence analysis, the feasibility of operation at overload is evaluated for the decoupled scheme against the state-of-art compensation technique and is shown to be a promising candidate for its simplicity and the lack of *preprocessing* of flux-map. All claims are experimentally validated on a 1.1 kW synchronous reluctance (SyR) machine test-bench.**

***Index Terms*—Sensorless control, signal injection, convergence analysis, synchronous reluctance machine.**

I. Introduction

Sensorless Control of synchronous reluctance (SyR) machines without a position transducer, also referred as encoderless or self-sensing, finds importance in industrial applications and automotive sector for cost and reliability benefits. The sensorless control techniques can be broadly classified into two categories [1]: *(i)* fundamental-wave excitation approach based on the back-emf integration for the non-zero speeds [2]–[4]; *(ii)* high-frequency excitation approach exploiting the differential saliences for the zero and low speeds region due to the poor observability of the back-emf signal [5]–[8]. The signal-injection sensorless control (SISC) falls in the latter category.

Over the years, many works on the SISC have pointed out the significance of magnetic saturation and the infamous cross-saturation position error [9]–[11]. Under load, the control operating point deviates away from the desired reference maximum-torque-per-ampere (MTPA) condition in the direction of decreasing saliency due to the cross-saturation error, leading to an eventual loss of control. Thus, the necessity for supplementary compensation techniques is recognized for the high load operations of saturated synchronous machines. For the known advantages of reduced torque ripples, the pulsating voltage injection along the estimated $\hat{d}$-axis is widely used over the rotating injection and the position error signal is designed proportional to the $\hat{q}$-axis high-frequency current; this remains the focus of this work.

This work was supported by the Power Electronics Innovation Center (PEIC) of Politecnico di Torino, Italy. *(Corresponding author: Anantaram Varatharajan)*

A. Varatharajan, G. Pellegrino and E. Armando are with the Department of Energy, Politecnico di Torino, Turin 10129, Italy. (email: anantaram.varatharajan@polito.it; gianmario.pellegrino@polito.it; eric.armando@polito.it)

Two types of compensation are commonly reported in literature: *(i)* an additive current compensation term to the position error signal at the input of the phase-locked-loop (PLL) [12], [13]; *(ii)* an additive angle compensation to the observed position at the output of the PLL, equivalent to the tilted axis injection [14]–[16]. The current compensation term proportional to the $\hat{d}$-axis high-frequency current is reported in [12], [13]; this is equivalent to replacing the q-axis high-frequency current with the corresponding q-axis flux estimate according to the motor current-model [9], [17]. A compensation term was added to the observed position as a representative of the cross-saturation error in [14], [15].

A comprehensive convergence analysis without the small-signal linearized approximation to assess the stability of SISC technique is evaluated in [18] for SyR machine and in [19], [20] for concentrated winding interior permanent magnet synchronous machine (IPMSM). To extend the operation to overload conditions beyond the rated torque, the two types of compensation are used together in synergy, i.e., additive current compensation with tilted voltage injection. Moreover, the spatial harmonics were taken into account by designing the compensation terms as a function of rotor position in [19], [20]

Alternative to the current compensation with tilted voltage injection, the paper proposes the use of a $\hat{q}$-axis current-model flux based position error signal which inherently decouples the two axes and compensates for the cross-saturation; this is referred to as the *decoupled position estimation* whose block diagram is shown in Fig. 1. The aim of this work is to subject the decoupled position estimation scheme to the

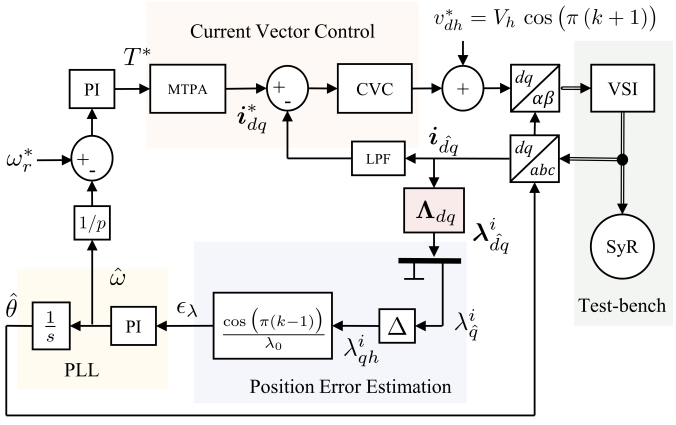

Fig. 1. Block diagram of the proposed decoupled signal-injection sensorless control system with the current-model flux based position estimation.

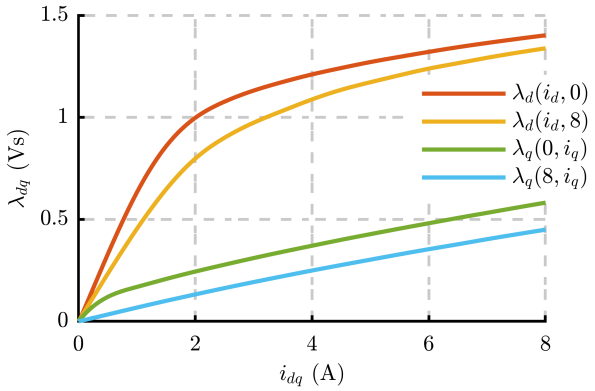

Fig. 2. Flux map of the 1.1 kW SyR motor under test exhibiting saturation and cross-saturation phenomenon. Experimentally identified with constant speed test reported in [21].

convergence analysis developed in [18]–[20] and to provide a comparison with the state-of-art compensation technique for extended overload operation in SISC.

Section II introduces the mathematical framework of the sensorless control system. The state-of-art compensation techniques for SISC under heavy saturation based on the convergence analysis are reviewed in Section III. The main contributions of this work described in Section IV are enumerated in the following:

1) The proposed decoupled scheme relies on the position estimation based on $\hat{q}$-axis current-model flux instead of the conventional $\hat{q}$-axis current and is subjected to the convergence analysis.
2) While the earlier works relied on convergence analysis to design the appropriate compensation techniques (namely the injection angle) for overload torque operations, the proposed method differs in that the convergence analysis is used only to demonstrate the stability but has no bearing on the design of the position observer.
3) This work demonstrates the stable overload torque capability of the proposed decoupled scheme (via convergence analysis) despite the simple and straightforward structure requiring no additional compensations.

The analytical evaluations are experimentally corroborated on a distributed winding SyR machine; the effect of spatial harmonics are overlooked. Section V presents the experimental results and Section VI concludes the paper.

II. Sensorless Control System

The electrical rotor position is θ and the electrical angular speed is $\omega = s\,\theta$ where s is the differential operation $\frac{\mathrm{d}}{\mathrm{d}t}$. Reference and Estimated vectors are represented by the superscript $\boldsymbol{x}^*$ and $\hat{\boldsymbol{x}}$, respectively. The orthogonal rotational matrix is $\mathbf{J} = \left[\begin{smallmatrix} 0 & -1 \\ 1 & 0 \end{smallmatrix}\right]$.

Real space vectors will be used; for example, the stator current is $\boldsymbol{i}_{dq} = [i_d\ i_q]^{\mathrm{T}}$ where i_d and i_q are the vector components in rotor reference frame. Space vectors in the stationary reference frame are denoted by the subscript $\alpha\beta$.

A. Synchronous Reluctance Machine Model

The machine model is expressed in the coordinates of the estimated rotor reference frame, denoted by subscript $\hat{dq}$, whose d-axis is at $\hat{\theta} = \theta - \tilde{\theta}$, where $\tilde{\theta}$ is the position error.

The voltage equation of a SyR machine in the estimated rotor reference frame is given by

$$s\,\boldsymbol{\lambda}_{\hat{dq}} = \boldsymbol{v}_{\hat{dq}} - R_s \boldsymbol{i}_{\hat{dq}} - \hat{\omega}\,\mathbf{J}\,\boldsymbol{\lambda}_{\hat{dq}} \tag{1}$$

where R_s is the stator resistance and $\boldsymbol{\lambda}_{\hat{dq}}$ is the stator flux linkage. The time derivative of the stator flux can be expressed with the incremental inductance matrix $\boldsymbol{L}_\partial$ as

$$s\,\boldsymbol{\lambda}_{\hat{dq}} = \mathrm{e}^{\mathbf{J}\tilde{\theta}}\,\boldsymbol{L}_\partial\,\mathrm{e}^{-\mathbf{J}\tilde{\theta}}\,s\,\boldsymbol{i}_{\hat{dq}} \qquad \boldsymbol{L}_\partial(\boldsymbol{i}_{dq}) = \begin{bmatrix} l_d & l_{dq} \\ l_{dq} & l_q \end{bmatrix} \tag{2}$$

where l_d, l_q represents the incremental inductance along direct d and quadrature q axis, respectively, while l_{dq} is the cross-saturation term. All inductances are functions of $\boldsymbol{i}_{dq}$. The electromagnetic torque is given by

$$T = \frac{3p}{2}\,\boldsymbol{i}_{\hat{dq}}^{\mathrm{T}}\,\mathbf{J}\,\boldsymbol{\lambda}_{\hat{dq}} \tag{3}$$

where p is the number of pole pairs.

B. Current-Model Flux-Map LUTs

Let $\boldsymbol{\Lambda}_{dq}(\boldsymbol{i}_{dq})$ denote the flux-map lookup tables (LUTs), shown in Fig. 2. Accurate parameters are assumed. Then, the real stator flux $\boldsymbol{\lambda}_{\hat{dq}}$ and the current-model stator flux estimate $\boldsymbol{\lambda}^i_{\hat{dq}}$ (denoted by the superscript i) can be expressed in the estimated rotor reference frame as

$$\boldsymbol{\lambda}_{\hat{dq}} = \mathrm{e}^{\mathbf{J}\tilde{\theta}}\,\boldsymbol{\Lambda}_{dq}(\boldsymbol{i}_{dq}) \qquad \boldsymbol{\lambda}^i_{\hat{dq}} = \boldsymbol{\Lambda}_{dq}(\boldsymbol{i}_{\hat{dq}}). \tag{4}$$

The current-model incremental inductance matrix $\boldsymbol{L}^i_\partial$ and its constituent terms are denoted by the superscript i and are retrieved in real-time from the flux-map LUTs; as an example:

$$l^i_d(\boldsymbol{i}_{\hat{dq}}) = \frac{\boldsymbol{\Lambda}_d(i_{\hat{d}} + \delta i_d, i_{\hat{q}}) - \boldsymbol{\Lambda}_d(i_{\hat{d}}, i_{\hat{q}})}{\delta i_d} \tag{5}$$

where δi_d is a small value (0.1 A). The other incremental inductances are computed in a similar fashion. As SyR machines have generally nonlinear magnetic model, the current-model incremental inductance is typically different from the real incremental inductance under non-zero position error, i.e.,

$$\tilde{\theta} \neq 0 \implies \boldsymbol{L}^i_\partial(\boldsymbol{i}_{\hat{dq}}) \neq \boldsymbol{L}_\partial(\boldsymbol{i}_{dq}). \tag{6}$$

C. Speed and Position Observer

A conventional phase lock loop (PLL) with a proportional-integral (PI) controller is employed to drive the position error signal ϵ to zero as

$$\hat{\omega} = k_p\,\epsilon + \int k_i\,\epsilon\,\mathrm{d}t \qquad \hat{\theta} = \int \hat{\omega}\,\mathrm{d}t \tag{7}$$

where k_p and k_i are the respective gains. The gains of the PLL are tuned for a critically damped response considering $\epsilon = \tilde{\theta}$ by placing the two poles at $s = -\Omega_\omega$:

$$k_p = 2\,\Omega_\omega \qquad k_i = \Omega_\omega^2. \tag{8}$$

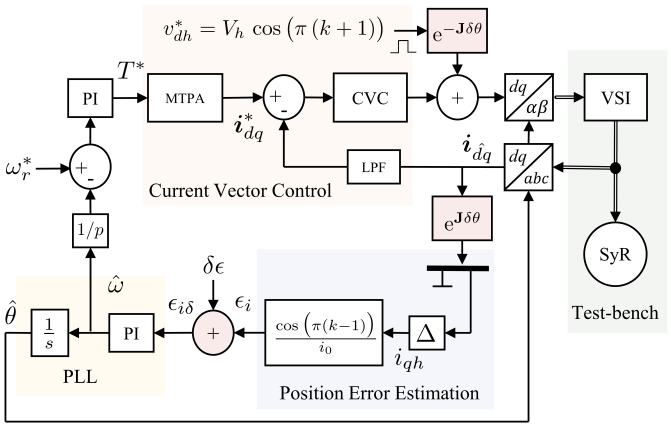

Fig. 3. Block diagram of the SISC system where the error compensation $\delta\epsilon$ and the injection angle $\delta\theta$ are also shown for generality.

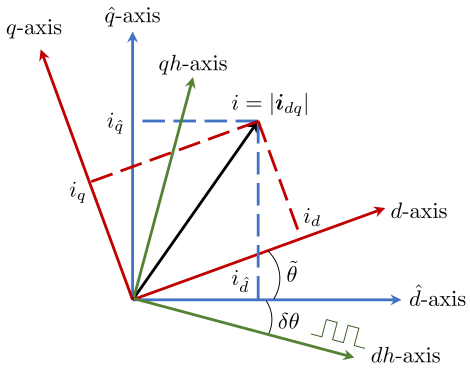

Fig. 4. Definition of the high-frequency injection reference frame dqh in relation to the estimated rotor reference frame $\hat{d}q$ and the real rotor reference frame dq.

III. Signal-Injection Sensorless Control

Let the superscript k denote the discrete domain representation of the k^{th} sampling instant. Let Δ symbolize the discrete difference operation as

$$\Delta x^k = x^k - x^{k-1}. \tag{9}$$

The block diagram of the SISC system is shown in Fig. 3 where the position error compensation $\delta\epsilon$ and the tilted injection angle $\delta\theta$ are also shown for generality.

A. Arbitrary Axis Voltage Injection

In the interest of generality, an arbitrary high-frequency injection reference frame dqh is considered that is phase shifted from the estimated reference frame $\hat{d}q$ by the injection angle $\delta\theta$, as shown in Fig 4. In this work, a pulsating voltage injection in the form of square-wave voltage at half the switching frequency is injected along the dh-axis, expressed as

$$v^k_{dh} = V_h \cos(\pi k) = \begin{cases} +V_h, & \text{if } k == 2n \\ -V_h, & \text{if } k == 2n+1 \end{cases} \tag{10}$$

where V_h is the magnitude and n is an integer. The square-ware injection is chosen for its ease of implementation and high-dynamic performance [22]. Nevertheless, the convergence analysis developed in the paper is also valid for the sinusoidal pulsating injection. Note that, due to the unit digital delay, the voltage actuated at the instant k corresponds to the reference computed at the instant $k-1$, i.e., $\boldsymbol{v}^k_{dq} = \left(\boldsymbol{v}^*_{dq}\right)^{k-1}$.

Conventionally, the position error signal ϵ is derived from the high-frequency current response in the direction orthogonal to the axis of injection, i.e., qh-axis current i_{qh}. It follows from (2) that

$$\boldsymbol{i}^k_{dqh} = e^{\mathbf{J}(\tilde{\theta}+\delta\theta)}\, \boldsymbol{L}^{-1}_{\partial}\, e^{-\mathbf{J}(\tilde{\theta}+\delta\theta)}\, \boldsymbol{\lambda}^k_{dqh} \tag{11}$$

where the high-frequency current corresponding to the square-wave voltage injection (10) is given by

$$\boldsymbol{i}^k_{dqh} = e^{\mathbf{J}\delta\theta}\, \Delta\, \boldsymbol{i}^k_{\hat{d}q}. \tag{12}$$

Typically, the stator resistance and the back-emf voltage terms are insignificant in the high-frequency domain and can be neglected, i.e.,

$$\boldsymbol{\lambda}^k_{dqh} = e^{\mathbf{J}\delta\theta}\, \Delta\, \boldsymbol{\lambda}^k_{\hat{d}q} \approx T_s \begin{bmatrix} v^{k-1}_{dh} \\ 0 \end{bmatrix} \tag{13}$$

where T_s is the sampling time interval. Simplifying (11), the high-frequency qh-axis current can be expressed as

$$i^k_{qh} = -\frac{T_s\, v^{k-1}_{dh} \sqrt{l^2_{\Delta} + l^2_{dq}}}{l_d l_q - l^2_{dq}} \sin\left(2\tilde{\theta} + 2\delta\theta - 2\tilde{\theta}_{dq}\right) \tag{14}$$

where $l_{\Delta} = \left(l_d - l_q\right)/2$ and $\tilde{\theta}_{dq}$ is the cross-saturation position error, defined as

$$\tilde{\theta}_{dq} = -\frac{1}{2} \tan^{-1} \frac{l_{dq}}{l_{\Delta}} \tag{15}$$

Unless explicitly mentioned otherwise, the superscript k is considered implicit in the following.

B. Conventional Position Estimation ($\delta\epsilon = 0$, $\delta\theta = 0$)

The conventional approach refers to the scheme with no compensation ($\delta\epsilon = 0$) and with the injection along the estimated $\hat{d}$-axis ($\delta\theta = 0$).

The high-frequency current i_{qh} (14) for the conventional position estimation becomes

$$i^k_{qh} = -\frac{T_s\, v^{k-1}_{dh} \sqrt{l^2_{\Delta} + l^2_{dq}}}{l_d l_q - l^2_{dq}} \sin\left(2\tilde{\theta} - 2\tilde{\theta}_{dq}\right) \tag{16}$$

Following (16), the conventional position error signal ϵ_i to the PLL (7) can be designed from i_{qh} as

$$\epsilon^k_i = \cos\left(\pi(k-1)\right) \frac{i^k_{qh}}{i_0} \tag{17}$$

where the gain i_0 is computed from the current-model incremental inductances for appropriate scaling as

$$i_0\left(\boldsymbol{i}_{\hat{d}q}\right) = -2\, T_s\, V_h \frac{\sqrt{(l^i_{\Delta})^2 + (l^i_{dq})^2}}{l^i_d l^i_q - (l^i_{dq})^2}. \tag{18}$$

It is emphasized that the gain i_0 is a function of the stator current in the estimated rotor reference frame $\boldsymbol{i}_{\hat{d}q}$, computed in real-time using (5).

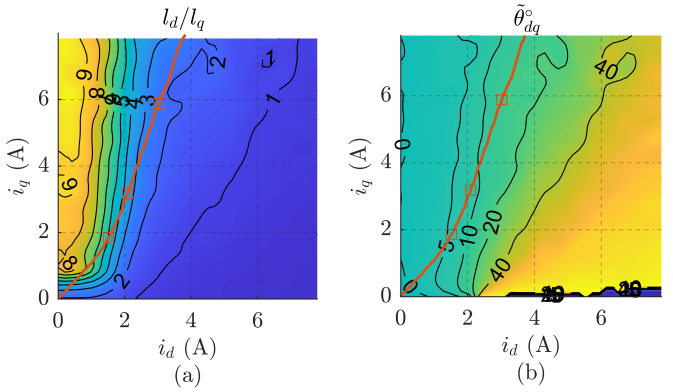

Fig. 5. (a) Incremental saliency in dq current plane of the SyR motor under test; (b) Cross-saturation position error (15) of the conventional position error signal. Red line is the MTPA trajectory. The markers denote the torque levels 0.5, 1 and 2 p.u.

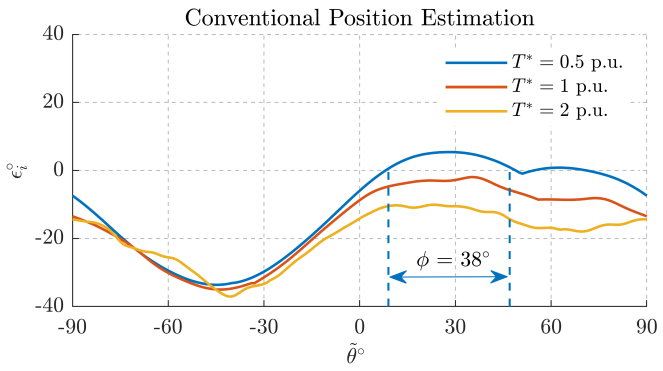

Fig. 6. Convergence analysis of the conventional position error signal (20) as a function of position error for three different torque references at MTPA operation.

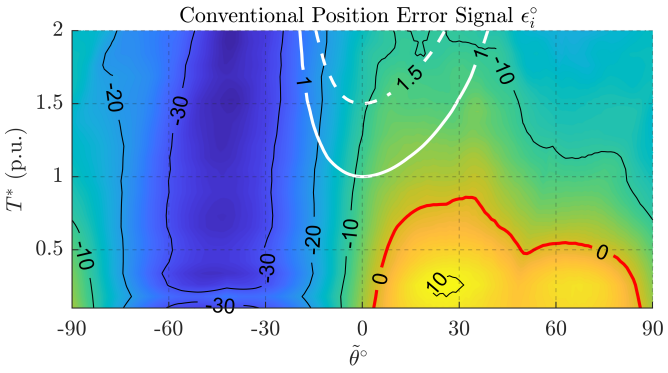

Fig. 7. Contour plot of the conventional position error signal (20) for the torque references at MTPA condition. Zero contour is highlighted in red. The white lines represent the torque output of 1 p.u. and 1.5 p.u. (dashed).

Due to the cross-saturation inductance l_{dq}, it is known that the conventional position error signal (17) incurs a steady-state position error which, equating the error signal (17) to zero, is equal to the cross-saturation error (15), i.e,

$$\epsilon_i = 0 \quad \Rightarrow \quad \tilde{\theta} = \tilde{\theta}_{dq} \tag{19}$$

The incremental saliency l_d/l_q in the dq current plane for the SyR motor under test is shown in Fig. 5(a) and the cross-saturation position error (15) in Fig. 5(b). It can be inferred that the position error diverges as the saliency weakens. Besides, it is observed that the position error progressively increases with load along the MTPA trajectory.

C. Convergence Analysis for Stability Assessment

To assess the stability of the control, a convergence analysis is developed by evaluating the position error signal as a function of position error [18]–[20], i.e., the error signal (17) can be expressed using (16) and (18) as

$$\epsilon_i = \overbrace{\frac{l_d^i l_q^i - (l_{dq}^i)^2}{2\sqrt{(l_\Delta^i)^2 + (l_{dq}^i)^2}}}^{f(\boldsymbol{i}_{\hat{dq}})} \cdot \overbrace{\frac{\sqrt{l_\Delta^2 + l_{dq}^2}}{l_d l_q - l_{dq}^2} \sin\left(2\tilde{\theta} - 2\tilde{\theta}_{dq}\right)}^{f(\boldsymbol{i}_{dq},\tilde{\theta})} \tag{20}$$

where the first term is a function of the current-model inductance $\boldsymbol{L}_\partial^i(\boldsymbol{i}_{\hat{dq}})$ referred to the estimated $\hat{dq}$ rotor reference frame while the second term is a function of the real inductance $\boldsymbol{L}_\partial(\boldsymbol{i}_{dq})$ and the position error. The convergence analysis is evaluated for the MTPA operating points as a function of torque reference, i.e.,

$$\boldsymbol{i}_{\hat{dq}} = \boldsymbol{i}_{dq}^*(T^*) \tag{21}$$

The zero crossing of the position error signal (20) with positive slope (zero-up crossing) is a stable equilibrium and a steady-state convergence point. The angular span in position error between the convergence point and the next zero-crossing is the stability buffer window, defined as the convergence margin ϕ.

Fig. 6 shows the convergence analysis for three different values of torque; the plot at half-rated reference torque ($T^* = 0.5$ p.u.) has a convergence point (steady-state position error) at $\tilde{\theta} = 9°$ with a convergence margin of about $\phi = 38°$. The higher torque curves have no zero-up crossings and thus, are unstable for the lack of a steady-state convergence of the PLL. For a comprehensive analysis, the contour of the conventional position error signal (20) is drawn as a function of torque in Fig. 7, where the zero level is highlighted in red to illustrate the absence of convergence points at rated torque and overload. In conclusion, the conventional position estimation scheme fails well before the rated torque condition for the machine under test.

IV. Compensation Techniques for Extending Operability

Various compensation techniques have been proposed to improve stability and to extend the operating range to beyond rated torque.

A. Compensated Position Estimation ($\delta\epsilon \neq 0$, $\delta\theta = 0$)

An offset in the form of error compensation $\delta\epsilon$ is added to the conventional position error signal ϵ_i (17), referred to as the compensated position error signal $\epsilon_{i\delta}$, to introduce a convergence point at the zero position error, i.e.,

$$\epsilon_{i\delta}\Big|_{\tilde{\theta}=0} = \epsilon_i + \delta\epsilon = 0 \tag{22}$$

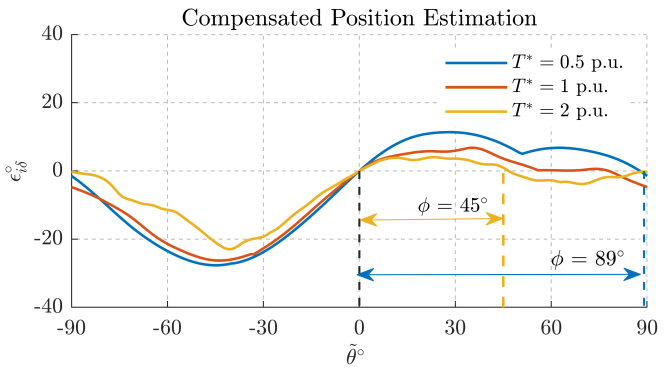

Fig. 8. Convergence analysis of the compensated position error signal (22) for three different reference torque at MTPA operation.

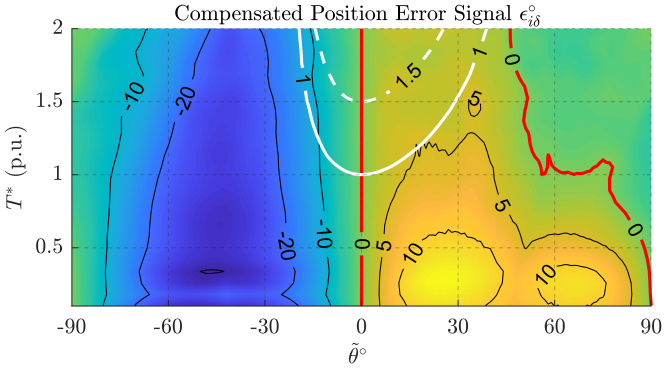

Fig. 9. Contour plot of the compensated position error signal (22) for the torque references at MTPA condition. Zero contour is highlighted in red. The white lines represent the torque output of 1 p.u. and 1.5 p.u. (dashed).

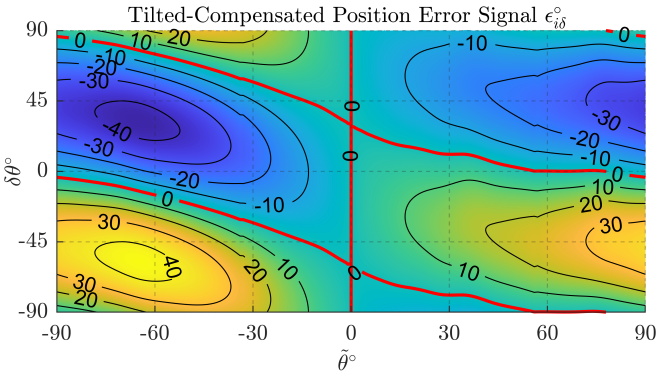

Fig. 10. Contour plot of the compensated position error signal (24) with tilted injection for the rated torque reference $T^* = 1$ p.u. at MTPA condition.

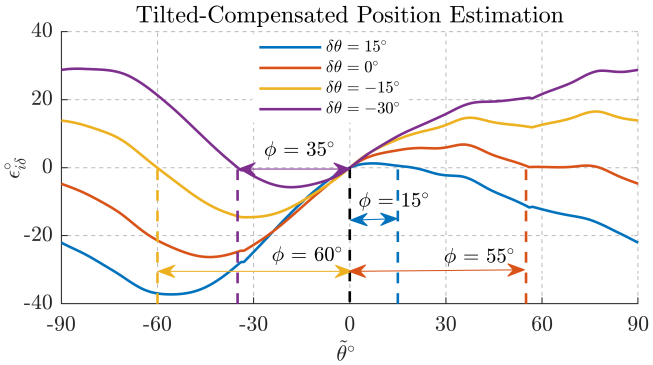

Fig. 11. Convergence analysis of the tilted-compensated position error signal (24) for the rated torque reference $T^* = 1$ p.u. at MTPA condition where the injection angle $\delta\theta = -15°$ has the largest convergence margin $\phi = 60°$.

It follows from (16)-(18) that the error compensation term $\delta\epsilon$ is given by

$$\delta\epsilon = \frac{1}{2}\sin(2\tilde{\theta}^i_{dq}) \tag{23}$$

where $\tilde{\theta}^i_{dq}$ is the cross-saturation position error (15) computed using the current-model inductance.

The convergence analysis plots for the compensated position estimation is shown in Fig. 8. With respect to Fig. 6, the curves in Fig. 8 have a dc-offset (23) to force the zero-up crossing at the zero position error. This is found to increase the convergence margin at the half-rated reference torque ($T^* = 0.5$ p.u.) from $\phi = 38°$ in Fig. 6 to $\phi = 89°$ in Fig. 8. At higher loads, although a zero-up crossing exists at zero position error, it is, at best, quasi-stable due to the poor convergence margin. It is better illustrated in the contour plot in Fig. 9 where, for the position error between $0° < \tilde{\theta} < 40°$ at overload, the corresponding position error signal is a plateau $\epsilon_{i\delta} < 5°$, implying poor capability and performance of sensorless control.

B. Tilted-Compensated Position Estimation ($\delta\epsilon \neq 0$, $\delta\theta \neq 0$)

The addition of error compensation $\delta\epsilon$ merely introduces an offset but the nature of the position error signal as a function of position error remains unaltered. Hence, the tilted frame injection is developed by changing the injection angle in conjunction with error compensation to explore the possibility of increasing the convergence margin [18]–[20]; this is considered the state-of-art.

For an injection angle $\delta\theta$, the high-frequency qh-axis current is defined in (14). Accordingly, the compensated position error signal for the tilted injection is given by

$$\epsilon^k_{i\delta} = \overbrace{\cos\big(\pi(k-1)\big)\frac{i^k_{qh}}{i_0}}^{\epsilon_i} + \overbrace{\frac{1}{2}\sin(2\tilde{\theta}^i_{dq} - 2\delta\theta)}^{\delta\epsilon} \tag{24}$$

where the error compensation $\delta\epsilon$ is a function of the injection angle $\delta\theta$ in addition to the current-model based cross-saturation error $\tilde{\theta}^i_{dq}$, equivalent to (23) of the former section.

The contour plot of the tilted-compensated position error signal (24) for different injection angles at rated torque reference $T^* = 1$ p.u. at MTPA condition is shown in Fig. 10 where the zero-up crossing (positive slope) at zero position error is obtained for the injection angles $-60° < \delta\theta < 20°$. Within this span, the optimal injection angle is chosen for maximizing the convergence margin. For a better representation, the results of convergence analysis in Fig. 10 is redrawn for selected injection angles in Fig. 11 where it can be discerned that the injection angle $\delta\theta = -15°$ provides the largest convergence margin ($\phi = 60°$) at the rated torque reference. The contour plot and the convergence analysis of the tilted-compensated position estimation at twice the rated torque reference ($T^* = 2$

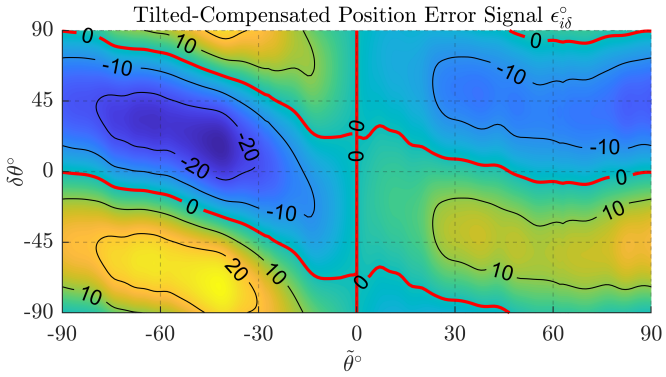

Fig. 12. Contour plot of the compensated position error signal (24) with tilted injection for twice the rated torque reference $T^* = 2$ p.u. at MTPA condition.

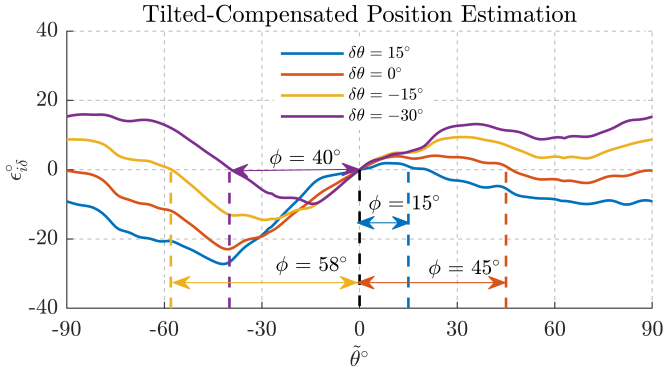

Fig. 13. Convergence analysis of the tilted-compensated position error signal (24) for twice the rated torque reference $T^* = 2$ p.u. at MTPA condition where the injection angle $\delta\theta = -15^{\circ}$ has the largest convergence margin $\phi = 58^{\circ}$.

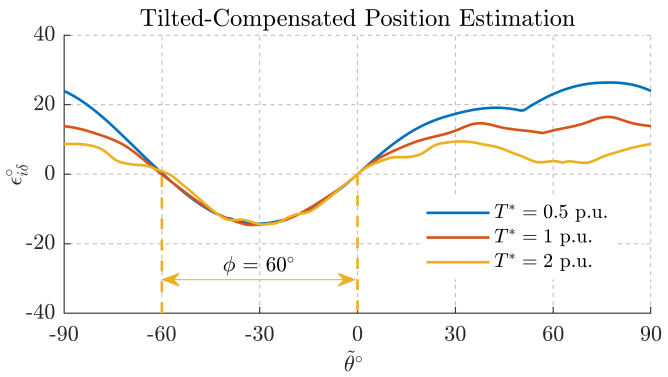

Fig. 14. Convergence analysis of the tilted-compensated position estimation (24) with an injection angle $\phi = -15^{\circ}$ for three different torque references at MTPA condition.

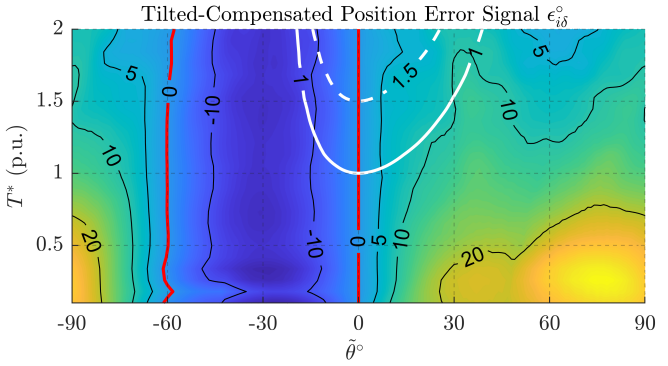

Fig. 15. Contour plot of the tilted-compensated position error signal (24) with an injection angle $\delta\theta = -15^{\circ}$ for different torque reference at MTPA condition. The white lines represent the torque output of 1 p.u. and 1.5 p.u. (dashed).

p.u.) is shown in Figs. 12 and 13, respectively. The slope of the position error signal at zero position error is reduced in Fig. 13 relative to Fig. 11. As before, the injection angle $\phi = -15^{\circ}$ is found to have the largest convergence margin.

Thus, the same injection angle is found suitable for all torque levels for the machine under test and is adopted for simplicity. Note that the injection angle carries the opposite sign ($\phi = 15^{\circ}$) for negative torque operation. To avoid discontinuity at zero load, the injection angle is linearly transitioned in the torque span ± 0.1 p.u. Fig. 14 shows the convergence analysis plots of the tilted-compensated position error signal at $\delta\theta = -15^{\circ}$ which is the counterpart of the compensated error signal in Fig. 8 ($\delta\theta = 0$); the increase in convergence margin is evident, thanks to the tilted injection. The contour plot of the tilted-compensated position error signal is shown in Fig. 15 where the plateau in the positive error quadrant in Fig. 9 is significantly improved and thus, increasing the convergence margin and stability.

However, the zero-up crossing slope is discerned to be steadily decreasing with load and the convergence curve at $T^* = 2$ p.u. in Fig. 14 is uncomfortably close to zero in the positive error plane. This presents a limitation to the tilted-compensated position estimation scheme. Moreover, the machine-dependent optimal tilt angle $\delta\theta = -15^{\circ}$ is unknown a priori and requires a significant engineering effort for calibration.

V. Proposed Decoupled Position Estimation

The signal-injection sensorless techniques discussed until now rely on the high-frequency current response that is orthogonal to the axis of voltage injection. However, the presence of cross-saturation phenomenon suggests that the orthogonal high-frequency current based position error signal is an inaccurate representation of the system and is susceptible to the cross-saturation error. It is shown that the qh-axis high-frequency current-model flux is a good candidate to design the position error signal [9], [17]. This is based on the observation that a high-frequency voltage signal injection on the exact d-axis produces by definition a flux aligned with the d-axis (immune to cross-saturation) where as the current response is misaligned due to the cross-saturation induced q-axis current.

The block diagram of the decoupled position estimation based on the current-model flux is shown in Fig. 1 where the simplicity of this technique is evidenced. As opposed to the state-of-art compensation techniques based on flux-map manipulation, the proposed scheme relies on a direct application of flux-map for the position error signal. The block $\mathbf{\Lambda}_{dq}$ represents the flux-map LUTs, according to the definition (4). The current-model or flux-map LUTs is often part of the

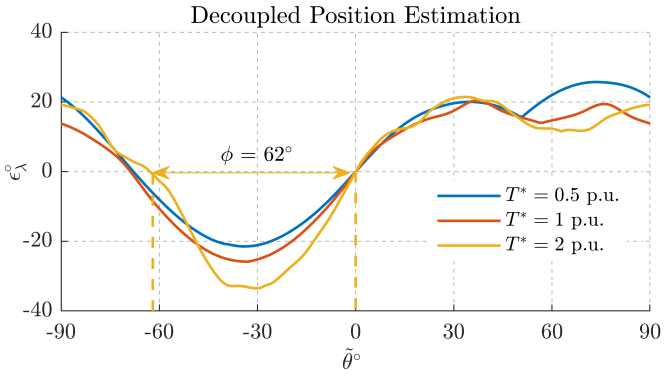

Fig. 16. Convergence analysis of the decoupled position error signal (27) as a function of position error for three different torque references at MTPA condition.

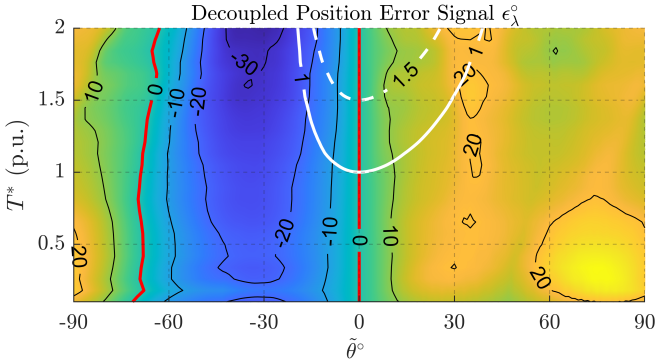

Fig. 17. Contour plot of the decoupled position error signal (27) for different torque references at MTPA condition. The white lines represent the torque output of 1 p.u. and 1.5 p.u. (dashed).

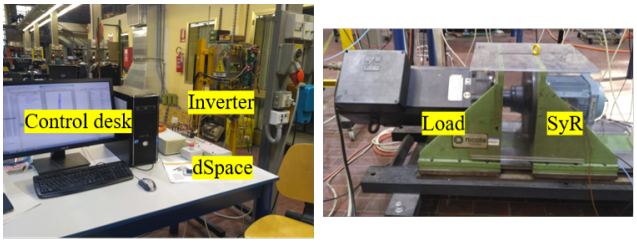

Fig. 18. Experimental Setup of 1.1 kW SyR motor under test on a dSPACE DS1103 control platform at a sampling frequency of 5 kHz.

flux observer that is integral for the fundamental-wave based sensorless control at higher speeds.

A. Error Signal Design

The feasibility of using the qh-axis high-frequency current-model flux λ^i_{qh} instead of the current i_{qh} is investigated, considering the straightforward injection angle $\delta\theta = 0$. From (2) and (4), the high-frequency response in current-model flux can be expressed as

$$\boldsymbol{\lambda}^i_{dqh} = \boldsymbol{L}^i_\partial \, \mathrm{e}^{\mathbf{J}\tilde{\theta}} \, \boldsymbol{L}^{-1}_\partial \, \mathrm{e}^{-\mathbf{J}\tilde{\theta}} \, \boldsymbol{\lambda}_{dqh}. \tag{25}$$

It can be discerned from (25) that λ^i_{qh} is a natural choice for position error signal as the zero position error is always a convergence point, i.e., $\lambda^i_{qh} = 0$ at $\tilde{\theta} = 0$. On expansion,

$$\lambda^i_{qh} = \frac{\lambda_{dh}}{l_d\, l_q - l^2_{dq}} \Big(-\sin(2\tilde{\theta}) \Big(l_\Delta \, l^i_q - l_{dq} \, l^i_{dq} \Big) + l^i_{dq} \Big(l_\Sigma - l_\Delta \, \cos(2\tilde{\theta}) \Big) - l^i_q \, l_{dq} \, \cos(2\tilde{\theta}) \Big) \tag{26}$$

where $l_\Sigma = (l_d + l_q)/2$. Linearizing (26), the decoupled position error signal is derived as

$$\epsilon^k_\lambda = \cos\big(\pi(k-1)\big) \frac{(\lambda^i_{qh})^k}{\lambda_0} \tag{27}$$

where the gain λ_0 is computed from the current-model incremental inductance in real-time for scaling as

$$\lambda_0 = -2\, T_s \, V_h \, \frac{l^i_\Delta \, l^i_q - (l^i_{dq})^2}{l^i_d \, l^i_q - (l^i_{dq})^2}. \tag{28}$$

Note that this scheme can be seen as a subset of the error compensation ($\delta\epsilon \neq 0$) where the compensating signal is proportional to the $\hat{d}$-axis high-frequency current i_{dh} [12], [13].

B. Convergence Analysis

Fig. 16 shows the curves of convergence analysis for different values of torque at MTPA condition for the decoupled scheme. Beside the zero-up crossing point at zero position error, a healthy convergence margin ($\phi \approx 70°$) is observed for all torque, including the overload operation as opposed to the tilted-compensation in Fig. 14.

The comprehensive contour plot of the decoupled position error signal is shown in Fig. 17 where the zero-up crossing at zero position error and the stable convergence margin are illustrated. Thus, without the need for any compensation and the preprocessing that accompanies it, the decoupled scheme is capable of handling overload operation while retaining simplicity in implementation.

VI. Experimental Results

The stability limits of the SISC techniques are evaluated experimentally with a 1.1 kW SyR motor (ABB 3GAL092513-BSB) on a dSPACE DS1103 control platform running at a sampling frequency of 5 kHz as shown in Fig. 18. The parameters of the SyR motor under test are shown in Table I.

The current controllers are tuned for a bandwidth of 100 Hz with damping coefficient of 1.58 (over-damped response). A

TABLE I
Motor Parameters

Parameters	Symbol	Values	Units
Rated power	P_n	1.1	kW
Rated voltage	V_n	340	V
Rated speed	ω_n	1500	rpm
Rated current	I_n	2.9	A
Rated torque	T_n	7.1	Nm
Pole pairs	p	2	-
Stator resistance	R_s	6.8	Ω
Shaft inertia	J	0.04	kgm^2

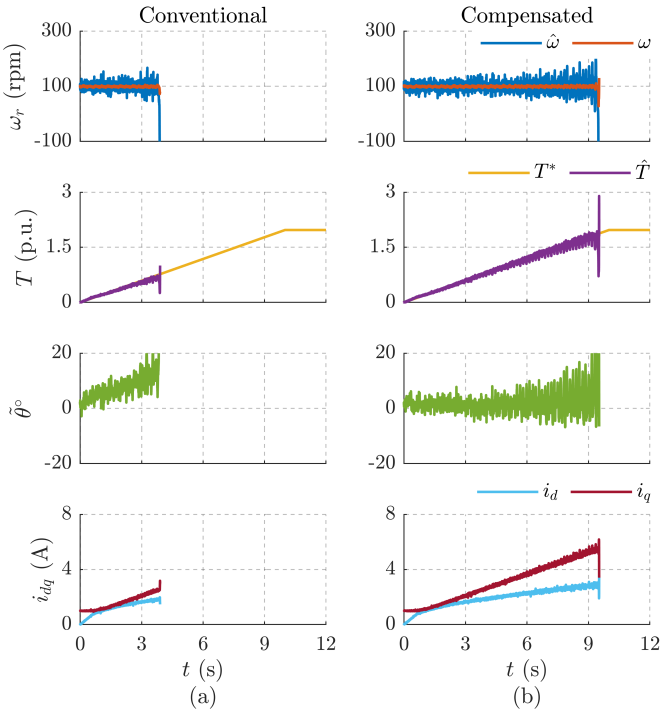

Fig. 19. Operational limit evaluation with a slow torque ramp $T = 0 \rightarrow 2$ p.u. at 100 rpm (0.06 p.u.): (a) Conventional position estimation; (b) Compensated position estimation.

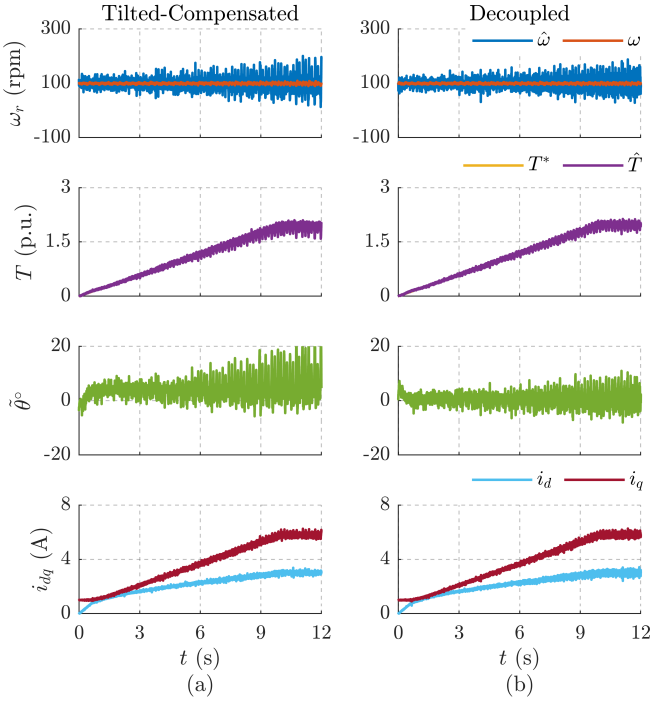

Fig. 20. Operational limit evaluation with a slow torque ramp $T = 0 \rightarrow 2$ p.u. at 100 rpm (0.06 p.u.): (a) Tilted-Compensated position estimation; (b) Decoupled position estimation.

minimum stator current $i_{q,min} = 1$ A (0.25 p.u.) is imposed for fundamental excitation at no load. The magnitude of the square-wave voltage injection is $V_h = 75$ V at half switching frequency of 2.5 kHz. A 13 bit magnetic encoder is used to evaluate the position error. The PLL gains are tuned for critical damping at $\Omega_\omega = 2\pi \cdot 15$ rad/s and the estimated speed is low-pass-filtered at 25 Hz. The motor under test is operated in the torque control mode and the speed is imposed by an auxiliary load machine. In the following results, the average torque $\hat{T}$ is estimated using the encoder and the flux-map of the machine under test.

A. Conventional Position Estimation

The operational limits of the conventional position estimation technique is evaluated in Fig. 19(a) with a slow torque ramp reference from zero to twice the rated ($T = 0 \rightarrow 2$ p.u.) at a low speed of 100 rpm. In accordance with Fig. 7, the position error is observed to increase with torque leading subsequently to the loss of control at $t = 3.8$ s for the maximum achievable torque $T = 0.6$ p.u.

B. Compensated Position Estimation

A similar test for operational limits evaluation for the compensated position estimation technique is shown in Fig. 19(b). The error compensation introduces a convergence point at the zero position error as discussed in Fig. 9; thus, the position error is approximately zero. At high overload, the diminished slope of the zero-up crossing in the positive error plane in Fig. 8 leads to the loss of control at $t = 9.4$ s for the maximum achievable torque $T = 1.7$ p.u.

C. Tilted-Compensated Position Estimation

The effectiveness of the tilted voltage injection ($\phi = -15°$) is evaluated for the slow ramp torque at 100 rpm in Fig. 20(a). Corroborating the analysis in Fig. 15, this scheme is able to achieve the overload of twice the rated torque. The position error shows some nervous behavior at high overload which is due to the poor signal quality in the positive error plane (see Fig. 14).

D. Decoupled Position Estimation

The performance of the decoupled technique for the similar torque ramp is shown in Fig. 20(b) where the overload capability at twice the rated torque is validated. In addition, the position error is relatively less nervous w.r.t Fig. 20(a) which can be attributed to the healthy zero-up crossing slope of the decoupled position error signal (see Fig. 16).

E. Overload Transient Response

The transient response to torque step ($T = 0 \rightarrow 2$ p.u.) and reversal ($T = 2 \rightarrow -2$ p.u.) at standstill condition for the tilted-compensated and the decoupled techniques is evaluated in Figs. 21(a) and 21(b), respectively. A small steady-state error ($\tilde{\theta} < 5°$ electrical) is observed under load; this is due to the average flux-map LUTs that do not represent the secondary saliences.

VII. Conclusion

This paper analyzed the prospect of the decoupled position estimation for overload operations under heavy saturation for a

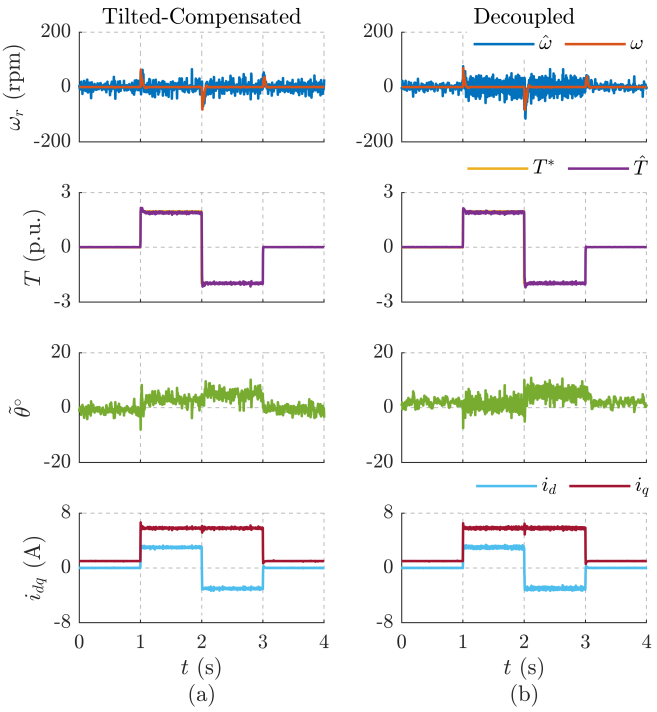

Fig. 21. Overload operation validation with torque step and reversal tests at standstill: (a) Tilted-Compensated position estimation; (b) Decoupled position estimation.

1.1 kW SyR machine. Once again, it was demonstrated that in presence of cross-saturation, the knowledge of the machine's flux-map LUTs is mandatory, as demonstrated by the lack of convergence of the conventional technique.

Following the review of state-of-art compensation techniques, the decoupled position estimation scheme was subjected to a similar convergence analysis for a comparative evaluation. It was shown that the decoupled scheme possesses good convergence margin and has a stable operation at overload on MTPA trajectory. Thus, given the simplicity and the lack of arduous preprocessing that the state-of-art compensation technique demands, the decoupled position estimation offers a promising alternative for SyR machines. In conclusion, the decoupled scheme does not require offline manipulation of the flux-map LUTs and it is thus the easiest to implement, by far, of all compensated schemes. The operational limits that are analytically evaluated were corroborated with experimental results.

References

[1] F. Briz and M. W. Degner, "Rotor Position Estimation," *IEEE Industrial Electronics Magazine*, vol. 5, no. 2, pp. 24–36, 2011.

[2] M. Hinkkanen, S. E. Saarakkala, H. A. A. Awan, E. Mölsä, and T. Tuovinen, "Observers for Sensorless Synchronous Motor Drives: Framework for Design and Analysis," *IEEE Transactions on Industry Applications*, vol. 54, no. 6, pp. 6090–6100, 2018.

[3] Y. Lee and S. K. Sul, "Model-Based Sensorless Control of an IPMSM With Enhanced Robustness Against Load Disturbances Based on Position and Speed Estimator Using a Speed Error," *IEEE Transactions on Industry Applications*, vol. 54, no. 2, pp. 1448–1459, 2018.

[4] A. Varatharajan and G. Pellegrino, "Sensorless Synchronous Reluctance Motor Drives: A General Adaptive Projection Vector Approach for Position Estimation," *IEEE Transactions on Industry Applications*, vol. 56, no. 2, pp. 1495–1504, 2020.

[5] P. L. Jansen and R. D. Lorenz, "Transducerless position and velocity estimation in induction and salient AC machines," *IEEE Transactions on Industry Applications*, vol. 31, no. 2, pp. 240–247, 1995.

[6] F. Briz, M. W. Degner, P. Garcia, and R. D. Lorenz, "Comparison of saliency-based sensorless control techniques for AC machines," *IEEE Transactions on Industry Applications*, vol. 40, no. 4, pp. 1107–1115, 2004.

[7] J. Holtz, "Acquisition of Position Error and Magnet Polarity for Sensorless Control of PM Synchronous Machines," *IEEE Transactions on Industry Applications*, vol. 44, no. 4, pp. 1172–1180, 2008.

[8] A. Varatharajan, P. Pescetto, and G. Pellegrino, "Sensorless Synchronous Reluctance Motor Drives: A Full-Speed Scheme using Finite-Control-Set MPC in a Projection Vector Framework," *IEEE Transactions on Industry Applications*, vol. 56, no. 4, pp. 3809–3818, 2020.

[9] E. Capecchi, P. Guglielmi, M. Pastorelli, and A. Vagati, "Position-sensorless control of the transverse-laminated synchronous reluctance motor," *IEEE Transactions on Industry Applications*, vol. 37, no. 6, pp. 1768–1776, 2001.

[10] N. Bianchi, E. Fornasiero, and S. Bolognani, "Effect of stator and rotor saturation on sensorless rotor position detection," in *IEEE Transactions on Industry Applications*, vol. 49, no. 3, 2013, pp. 1333–1342.

[11] D. Mingardi, M. Morandin, S. Bolognani, and N. Bianchi, "On the Proprieties of the Differential Cross-Saturation Inductance in Synchronous Machines," *IEEE Transactions on Industry Applications*, vol. 53, no. 2, pp. 991–1000, 2017.

[12] Y. Li, Z. Q. Zhu, D. Howe, C. M. Bingham, and D. A. Stone, "Improved Rotor-Position Estimation by Signal Injection in Brushless AC Motors, Accounting for Cross-Coupling Magnetic Saturation," *IEEE Transactions on Industry Applications*, vol. 45, no. 5, pp. 1843–1850, 2009.

[13] T. Tuovinen and M. Hinkkanen, "Adaptive Full-Order Observer With High-Frequency Signal Injection for Synchronous Reluctance Motor Drives," *IEEE Journal of Emerging and Selected Topics in Power Electronics*, vol. 2, no. 2, pp. 181–189, 2014.

[14] Z. Q. Zhu, Y. Li, D. Howe, and C. M. Bingham, "Compensation for Rotor Position Estimation Error due to Cross-Coupling Magnetic Saturation in Signal Injection Based Sensorless Control of PM Brushless AC Motors," in *2007 IEEE International Electric Machines & Drives Conference*, vol. 1, 2007, pp. 208–213.

[15] Y. Lee, Y. Kwon, S. Sul, N. A. Baloch, and S. Morimoto, "Compensation of position estimation error for precise position-sensorless control of IPMSM based on high-frequency pulsating voltage injection," in *2017 IEEE Energy Conversion Congress and Exposition (ECCE)*, 2017, pp. 859–864.

[16] S. Kuehl, P. Landsmann, and R. M. Kennel, "Compensating angle estimation errors caused by magnetic saturation in anisotropy-based sensorless control schemes," in *3rd IEEE International Symposium on Sensorless Control for Electrical Drives (SLED 2012)*, 2012, pp. 1–6.

[17] A. Varatharajan, G. Pellegrino, and E. Armando, "Sensorless synchronous reluctance motor drives: Auxiliary flux based position observer," *IEEE Journal of Emerging and Selected Topics in Power Electronics*, pp. 1–10, 2020.

[18] V. Manzolini and S. Bolognani, "On the Rotor Position Self-Sensing Capability of Reluctance and IPM Synchronous Motors," *IEEE Transactions on Industry Applications*, vol. 56, no. 4, pp. 3755–3766, 2020.

[19] Y. Kwon, J. Lee, and S. Sul, "Extending Operational Limit of IPMSM in Signal-Injection Sensorless Control by Manipulation of Convergence Point," *IEEE Transactions on Industry Applications*, vol. 55, no. 2, pp. 1574–1586, 2019.

[20] J. Lee, Y. Kwon, and S. Sul, "Signal-Injection Sensorless Control With Tilted Current Reference for Heavily Saturated IPMSMs," *IEEE Transactions on Power Electronics*, vol. 35, no. 11, pp. 12 100–12 109, 2020.

[21] E. Armando, R. I. Bojoi, P. Guglielmi, G. Pellegrino, and M. Pastorelli, "Experimental identification of the magnetic model of synchronous machines," *IEEE Transactions on Industry Applications*, vol. 49, no. 5, pp. 2116–2125, 2013.

[22] Y. D. Yoon, S. K. Sul, S. Morimoto, and K. Ide, "High-bandwidth sensorless algorithm for AC machines based on square-wave-type voltage injection," *IEEE Transactions on Industry Applications*, vol. 47, no. 3, pp. 1361–1370, 2011.